ORIGINAL PAPER

Quadrupole magnet design based on genetic multi-objective optimization

Eric Diehl[1] · Moritz von Tresckow[1] · Lou Scholtissek[1] · Dimitrios Loukrezis[1] · Nicolas Marsic[1] ·
Wolfgang F. O. Müller[1] · Herbert De Gersem[1]

Abstract
This work suggests to optimize the geometry of a quadrupole magnet by means of a genetic algorithm adapted to solve
multi-objective optimization problems. To that end, a non-domination sorting genetic algorithm known as NSGA-III is used.
The optimization objectives are chosen such that a high magnetic field quality in the aperture of the magnet is guaranteed,
while simultaneously the magnet design remains cost-efficient. The field quality is computed using a magnetostatic finite
element model of the quadrupole, the results of which are post-processed and integrated into the optimization algorithm.
An extensive analysis of the optimization results is performed, including Pareto front movements and identification of best
designs.

Keywords Magnet design · Quadrupole · Geometry optimization · Multi-objective optimization · Genetic algorithm ·
NSGA-III

1 Introduction

Multipole magnets are essential components of particle
accelerators and are of paramount importance for the success of particle physics experiments that are performed in
accelerator facilities [1]. Quadrupole magnets, in particular, are crucial for keeping particle beams focused on their
desired trajectories [2]. The very nature of particle physics
experiments places very high demands on the operation and
performance of accelerator magnets. Therefore, their production must be based on meticulous design procedures.

Focusing on the case of quadrupole magnet design, common practice dictates to formulate the design objectives
into an optimization problem with respect to the geometric parameters of the quadrupole, while certain operational
parameters must also be taken into account during the optimization process. Therein, the electromagnetic phenomena
taking place inside the magnet are typically simulated using a
digital magnet model and are included into the optimization
as performance measures [3–7]. However, such geometry

optimization problems are notoriously hard to solve, in fact,
NP-hard [8], due to the fact that their computational complexity increases exponentially with the number of solution
candidates. In many cases, the only viable option is to
employ search algorithms that are capable of comprehensively exploring the parameter space and finding an adequate
configuration at a reasonable computational cost. Popular
methods of choice are Monte Carlo algorithms [9–11], simulated annealing [12, 13] or genetic algorithms (GAs) [14–17],
all of which have been successfully applied to a number of
geometry optimization problems [18–20].

This work focuses on the use of GAs for the purpose
of quadrupole design. Originally, GAs have been developed for unconstrained, single-objective optimization problems, which constitute their natural domain of application
[21]. However, most geometry optimization applications,
also including quadrupole magnet design, feature multiple
and often conflicting objectives. In such cases, a multi-objective optimization (MOO) [22, 23] must be solved
instead. Therein, the goal is to find so-called *Pareto optimal*
solutions, which cannot be further improved with respect to
one objective without worsening another [24]. Such MOO
problems are faced and tackled increasingly more often in
various engineering applications that concern geometry optimization [25–28]. To address these problems, traditional

✉ Moritz von Tresckow
  moritz.von_tresckow@tu-darmstadt.de

1 Institute for Accelerator Science and Electromagnetic Fields
   (TEMF), Technische Universität Darmstadt, Schlossgartenstr.
   8, 64289 Darmstadt, Germany

GAs have been extended, e.g., in the form of so-called non-dominated sorting genetic algorithms (NSGAs) [29–32].

Regarding the quadrupole magnet design problem considered in this work, the objectives of the MOO are: (a) the maximization of magnetic field quality within the aperture of the quadrupole magnet and (b) the minimization of the magnet's radius. The former objective is aligned with the desired magnet operation with respect to beam focusing. The latter objective aims at designs that use the minimum necessary amount of magnet material, so that production costs remain acceptable. The magnetic field quality is first computed using a magnetostatic finite element (FE) magnet model and then expressed in the form of relative multipole coefficients on a reference radius. The evaluation of the relative multipole coefficients is integrated into the fitness function of an NSGA, such that only solutions which maximize the magnetic field quality are allowed to propagate through the evolution process, as dictated by the first optimization objective. In particular, the algorithm known as NSGA-III [31] is employed. The solutions are further constrained by the second objective, i.e., the need for a minimal magnet radius. The Pareto optimal solutions, i.e., those that provide an acceptable balance with respect to both objectives, are then analyzed such that the best magnet design candidates are identified.

While works featuring GA-based MOO algorithms for the optimization of accelerator systems do appear in the literature [33–38], the application of such optimization algorithms to accelerator magnet design seems to have been so far neglected. In fact, the only relevant work that the authors are aware of is [1], which mentions the option of optimizing accelerator magnets by means of MOO based on GAs, however, without providing any verification in the form of numerical experiments. The present work aims to fill this gap.

The rest of this paper is organized as follows. Section 2 presents the problem formulation with respect to computing the magnetic field of the magnet for a given design, the magnet model considered in this work, and the computation of the magnetic field quality in the aperture of the magnet. Section 3 presents the general formulation of MOO problems and discusses GAs suitable for the solution of such problems, in particular the NSGA-III. In Sect. 4, the MOO problem with respect to the quadrupole magnet design is formulated. The numerical results obtained by means of the NSGA-III algorithm are presented and extensively discussed in Sect. 5. Finally, conclusions are drawn in Sect. 6.

2 Problem formulation and magnet model

The physical behavior of a quadrupole magnet can be fully described by the Maxwell equations, which provide the math-

ematical foundation for classical electrodynamics. However, in most cases, it suffices to provide an approximate description of the electromagnetic phenomena appearing in a given problem setting, thus simplifying the underlying equations and the resulting simulation model. For our particular application of a quadrupole magnet with nonlinear materials, it is sufficient to consider a magnetostatic representation of the underlying magnetic field quantities. Therefore, we employ the magnetic vector potential formulation in the steady-state regime.

Considering the 3D case, the magnetic vector potential formulation is given as

$$\nabla \times (\nu(\mathbf{b})\nabla \times \mathbf{a}) = \mathbf{j}, \tag{1}$$

where ν is the magnetic reluctivity tensor, $\mathbf{b}$ the magnetic flux density, $\mathbf{a}$ the magnetic vector potential, and $\mathbf{j}$ the current density. Equation (1) is discretized by employing a projection on (1) with a test function $\mathbf{v}$ on a computational domain Ω with boundary $\partial\Omega = \partial\Omega_N \cup \partial\Omega_D$, where $\partial\Omega_N$ and $\partial\Omega_D$, respectively, denote the boundary parts where Neumann and Dirichlet boundary conditions (BCs) are imposed [39]. The corresponding weak formulation reads:

Find $\mathbf{a} \in \mathbf{L}_0(\mathrm{curl}, \Omega)$ such that

$$\int_\Omega \nu(\mathbf{b})\nabla \times \mathbf{a} \cdot \nabla \times \mathbf{v}\, d\Omega = \int_\Omega \mathbf{j} \cdot \mathbf{v}\, d\Omega, \tag{2}$$

for all test functions $\mathbf{v}$ in the space $\mathbf{L}_0(\mathrm{curl}, \Omega)$, defined as

$$\mathbf{L}_0(\mathrm{curl}, \Omega) = \{\mathbf{u} \in \mathbf{H}(\mathrm{curl}, \Omega) : \mathbf{n} \times \mathbf{u} = 0|_{\partial\Omega_D}\}. \tag{3}$$

In (3), $\mathbf{H}(\mathrm{curl}, \Omega)$ is the space of square-integrable functions with square-integrable weak curl. Note that the Neumann boundary integral arising in the deduction of (2) vanishes by applying the Neumann BC $\mathbf{n} \cdot (\nu(\mathbf{b})\,\mathbf{b}) = 0$, where $\mathbf{n}$ is the outer normal unit vector. The Dirichlet BC $\mathbf{n} \times \mathbf{a} = 0$ is enforced in $\mathbf{L}_0(\mathrm{curl}, \Omega)$.

The magnetic vector potential is approximated within a finite element space as

$$\mathbf{a} = \sum_{j=1}^{E} \hat{a}_j \mathbf{w}_j, \tag{4}$$

where $\hat{a}_j$ are the degrees of freedom (dofs), E is the number of dofs, and $\mathbf{w}_j$ denotes Nédélec basis functions of the first kind and the first order [40]. We apply the Ritz–Galerkin procedure, such that the set of test functions is the same as the set of shape (basis) functions.

2.1 2D magnet model

The magnet model is further simplified taking into account the translation invariance of the magnet along the z-axis. Therefore, we may consider a magnetic vector potential perpendicular to a 2D cross section of the 3D domain, in which case $\mathbf{a} = [0, 0, a_z = a_z(x, y)]^\top$ and $\mathbf{j} = [0, 0, j_z]^\top$. We denote the computational domain of the 2D cross section of the quadrupole magnet with $\Omega_{2D} := \{\mathbf{x} \in \mathbb{R}^2 \mid \|\mathbf{x}\|_2 \le R\}$, which corresponds to a circle with radius $R \in \mathbb{R}$ around the origin. Figure 1 depicts the full 2D quadrupole magnet model contained in Ω_{2D}, where the corresponding geometry descriptors and numerical identifiers are given in Table 1. The Dirichlet BC $\mathbf{n} \times \mathbf{a} = 0$ is imposed on the boundary $\partial\Omega_D$, also shown in Fig. 1.

Table 1 also presents the intervals $[a_i, b_i]$, within which the geometrical parameters are allowed to vary during the optimization procedure, i.e., $a_i \le x_i \le b_i$, $i = 1, \ldots, 6$. Parameters with constant values throughout the optimization are denoted with the identifiers A and B. Shims are included in the quadrupole model as important pole adjustments, which can lead to significant improvements in the homogeneity of the magnetic field, thus, to field quality improvements as well [41]. Further improvements can also be achieved through pole shape optimization as in [42]. The nonlinear material of the yoke and the poles is modeled with a

Brauer curve approximation [43] upon 1010-Steel and implemented in a FE solver with the Newton method [44]. The model is implemented using three open-source tools, namely the mesh generator `Gmsh` [45], the `GetDP` FE solver [44], and the `ONELAB` interface [46].

2.2 Convergence of the finite element discretization

The convergence of the FE discretization of the magnet model is investigated by solving Equation (1) for a repeatedly finer 2D mesh, while for each refinement step the magnetic energy in the computational domain Ω is post-processed. Figure 2 depicts the resulting relative error of the magnetic energy over the number of dofs, indicating a first-order polynomial convergence with respect to the number of 2D mesh nodes. For the further results in this paper, the magnetostatic problem is solved with 18665 2D mesh nodes and 9081 triangular elements for each model evaluation of the quadrupole magnet.

2.3 Aperture field quality

One of the most important quantities of interest to be taken into account during the design of a quadrupole magnet is the field quality here represented by the harmonic distortion factor Q, which can be computed upon the multipole coef-

Fig. 1 2D cross section of the quadrupole magnet. The computational domain, its boundaries, and the different material-based subdomains are presented as in the legend. The identifiers $1 - 6$ and the letters A, B, denote the geometrical parameters of the magnet, as described in Table 1 (color figure online)
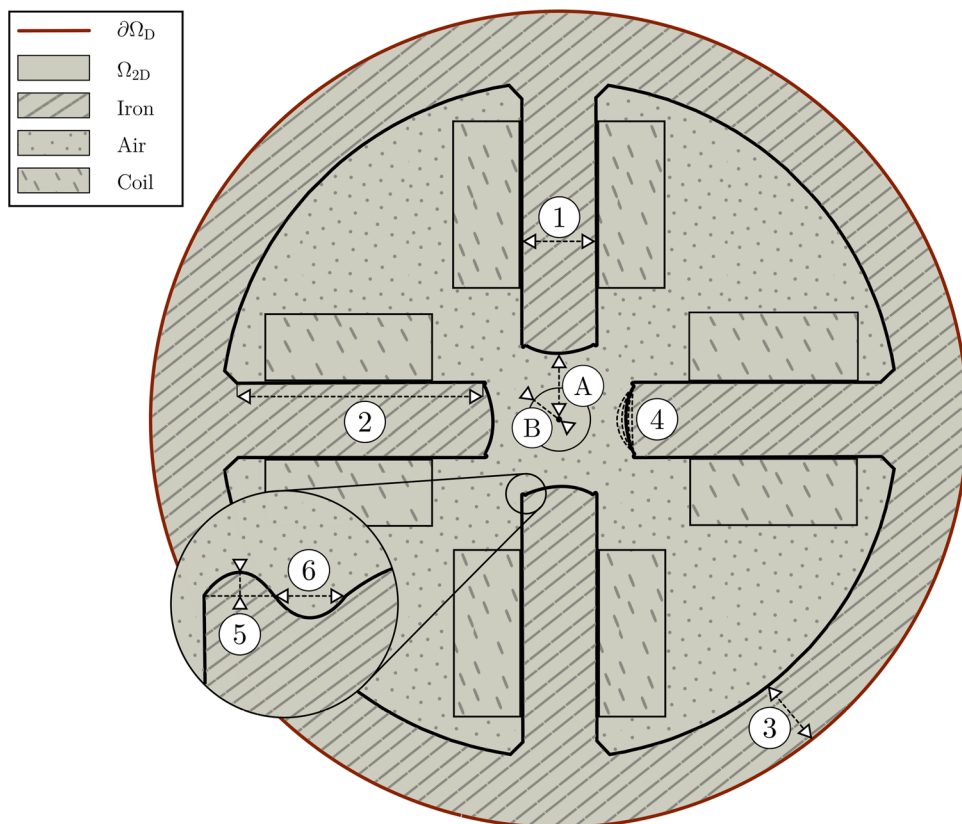
ficients of the calculated field in the magnet's aperture. The harmonic distortion factor captures the relationship between the desired multipoles such as the quadrupole components, and undesired multipoles such as duodecapole components and higher-order terms. Therefore, Q is a measure for the magnetic field quality of the quadrupole magnet and can be calculated as follows: The FE solution a_z is evaluated at a reference circle with radius r_{ref}. The result is then represented by a Fourier series with Fourier coefficients a_p and b_p, such that

$$a_z(r_{\text{ref}}, \varphi) = \sum_{p=0}^{\infty} \left(a_p \cos(p\varphi) + b_p \sin(p\varphi) \right), \quad (5)$$

using the polar coordinate system (r, φ). Then, the Fourier characterization of the magnetic vector potential and the magnetic flux density in the beam aperture are given as [1]

$$a_z(r, \varphi) = \sum_{p=0}^{\infty} \left(\frac{r}{r_{\text{ref}}} \right)^p \left(a_p \cos(p\varphi) + b_p \sin(p\varphi) \right), \quad (6)$$

$$b_r(r, \varphi) = \sum_{p=1}^{\infty} \left(\frac{r}{r_{\text{ref}}} \right)^p \frac{p}{r} \left(-a_p \sin(p\varphi) + b_p \cos(p\varphi) \right), \quad (7)$$

$$b_\varphi(r, \varphi) = \sum_{p=1}^{\infty} \left(\frac{r}{r_{\text{ref}}} \right)^p \frac{p}{r} \left(-a_p \cos(p\varphi) - b_p \sin(p\varphi) \right). \quad (8)$$

The evaluation at $r = r_{\text{ref}}$ for the radial magnetic flux density yields

$$b_r(r_{\text{ref}}, \varphi) = \sum_{p=1}^{\infty} \left(\underbrace{-a_p \frac{p}{r_{\text{ref}}} \sin(p\varphi)}_{B_p(r_{\text{ref}})} + \underbrace{b_p \frac{p}{r_{\text{ref}}} \cos(p\varphi)}_{A_p(r_{\text{ref}})} \right), \quad (9)$$

where B_p and A_p are called *normal* and *skew harmonic coefficients*, respectively. The harmonic distortion factor $Q(r_{\text{ref}})$ in the aperture of a $2P$-pole magnet considered at a reference radius r_{ref} can be obtained from the harmonic Fourier coefficients using the formula [1]

$$Q_P(r_{\text{ref}}) = \frac{1}{A_P^2(r_{\text{ref}})} \sum_{\substack{p=1 \\ p \neq P}}^{\infty} \left(B_p^2(r_{\text{ref}}) + A_p^2(r_{\text{ref}}) \right). \quad (10)$$

For a quadrupole magnet ($P = 2$), with a quadrupole field gradient

$$g(r) = A_2(r), \quad (11)$$

Table 1 Geometrical parameters of the quadrupole magnet

Description	Identifier	Notation	Value	Units
Pole width	①	x_1	[14.0, 20.0]	mm
Pole height	②	x_2	[45.0, 120.0]	mm
Yoke height	③	x_3	[10.0, 25.0]	mm
Pole bending[1]	④	x_4	[0.03, 0.1]	–
Shim height	⑤	x_5	[0.1, 0.55]	mm
Shim width	⑥	x_6	[0.4, 1.2]	mm
Bore radius	Ⓐ	–	15.0	mm
Reference radius	Ⓑ	r_{ref}	11	mm

The pole tip profile is modeled using a B-spline that is dependent on the design variable x_4. Only the radial coordinate of the resulting parametrization is proportional to x_4. Accordingly, in the case of the $\frac{1}{8}$-th quadrupole, $x \propto \text{acosh}(cx_4)$
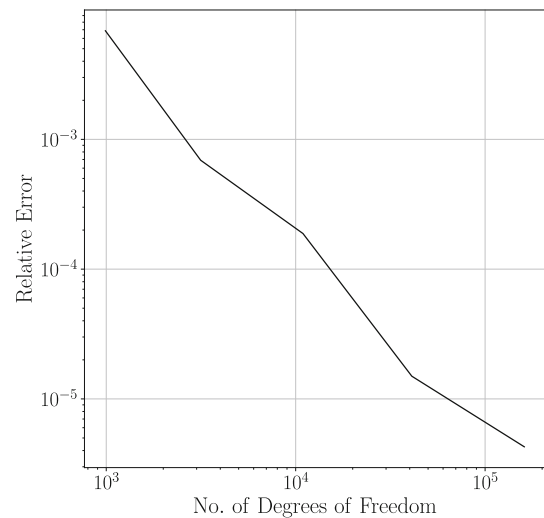

Fig. 2 Convergence of the FE discretization. Four refinements of the 2D FE mesh have been executed, ranging from 990 dofs to 161028 dofs (color figure online)

the magnetic field should be close to a pure quadrupole field, i.e., the field gradient g should be high in comparison with the other multipole coefficients A_p, with $p = 1, \ldots, C$, and $p \neq 2$, where C refers to the truncation coefficient. Accordingly, the corresponding harmonic distortion factor for a quadrupole magnet, given by

$$Q_2(r_{\text{ref}}) = \frac{1}{g^2(r_{\text{ref}})} \sum_{\substack{p=1 \\ p \neq 2}}^{C} \left(B_p^2(r_{\text{ref}}) + A_p^2(r_{\text{ref}}) \right), \quad (12)$$

should be in the order of 10^{-4} [1].

3 Multi-objective optimization

In MOO, we seek to minimize (or maximize, depending on the problem at hand) a set of—possibly conflicting—objective functions $f_i(\mathbf{x}) : \mathcal{X} \rightarrow \mathbb{R}$, $i = 1, ..., k$, $k \geq 2$, where $\mathbf{x} = (x_1, \ldots, x_n) \in \mathcal{X}$ denotes the vector of decision variables, equivalently, optimization parameters, and the domain $\mathcal{X} \subset \mathbb{R}^n$ is referred to as the *feasible decision region* [22, 23]. For a feasible parameter vector $\mathbf{x} \in \mathcal{X}$, a corresponding feasible objective vector $\mathbf{z} = (f_1(\mathbf{x}), \ldots, f_k(\mathbf{x}))$ is obtained, where $\mathbf{z} \in \mathcal{Z}$ and $\mathcal{Z} \subset \mathbb{R}^k$ is called the *feasible objective region*.

The structure of $\mathcal{X}$ is induced by a set of constraints applied to the decision variables. In the specific case of geometry optimization, these constraints are often given in the form of bounding box intervals, similar to the ones shown in Table 1, such that $\mathcal{X} := [a_1, b_1] \otimes \cdots \otimes [a_n, b_n]$, where $a_i \leq x_i \leq b_i$, $i = 1, \ldots, n$. Given this set of constraints, the MOO problem reads

$$\min_{\mathbf{x} \in \mathcal{X}} \{f_1(\mathbf{x}), ..., f_k(\mathbf{x})\}. \tag{13}$$

In most cases, a parameter vector that minimizes all objective functions simultaneously does not exist. It is therefore necessary to have a method of comparing a set of solutions while taking into account the satisfaction of all objectives. This issue is resolved using the concept of *dominating solutions*. Assuming two parameter vectors $\mathbf{x}, \tilde{\mathbf{x}} \in \mathcal{X}$ arising in a minimization procedure, then $\tilde{\mathbf{x}}$ dominates $\mathbf{x}$ if

$$f_i(\tilde{\mathbf{x}}) < f_i(\mathbf{x}) \text{ and } f_j(\tilde{\mathbf{x}}) \leq f_j(\mathbf{x}), \forall i, j \in \{1, ..., n\}, i \neq j. \tag{14}$$

A parameter vector that cannot be dominated is called *Pareto optimal* [24]. In essence, Pareto optimality means that the current solution cannot be further improved with respect to one of the objectives, without simultaneously deteriorating another objective. The set of Pareto optimal solutions is referred to as the *Pareto front*. A Pareto front is bounded by the *ideal* and *nadir* objective vectors, respectively, denoted with $\mathbf{z}^*$ and $\mathbf{z}^{\text{nad}}$. The former is obtained by individually optimizing the objective functions and the latter by approximating the worst objective values of the Pareto front.

3.1 Genetic algorithms

GAs belong to a class of population based, stochastic optimization algorithms which solve optimization problems by only allowing candidate solutions with a promising "gene pool" to reproduce and propagate through generations $t = 1, 2, \ldots, T$, where T is the final generation [15, 16]. This generation-based evolution of candidates is realized by creating a sequence of subsets $\mathcal{P}$ in the feasible decision space

called *populations*, which eventually converge to a set of minimizers. In that way, a sequence $(\mathcal{P}_t)_{t\in\mathbb{N}} \subset \mathcal{X}$ with

$$\mathcal{P}_t \xrightarrow{t \rightarrow \infty} \mathcal{P}^* \tag{15}$$

is generated, such that each $\mathbf{x} \in \mathcal{P}^*$ is a minimizer of (13). To deal with the limitations of realistic and thus finite calculations, Equation (15) needs to be truncated by a final generation T, so that with

$$\mathcal{P}_t \xrightarrow{t \rightarrow T} \mathcal{P}_T, \tag{16}$$

a set of generation-related minimizers $\mathbf{x} \in \mathcal{P}_T$ is considered.

The sequence of populations $(\mathcal{P}_t)_{t=1,2,...,T}$ is dictated by the genetic operators *crossover* C_σ, *mutation* M_r, and *fitness selection* F, such that

$$\mathcal{P}_{t+1} = F \circ M_m \circ C_\sigma (\mathcal{P}_t), \tag{17}$$

where $\circ$ expresses the concatenation of the sequentially applied genetic operators on the current population $\mathcal{P}_t$. The indices σ and m, respectively, denote the crossover and mutation rates of the corresponding operators, where $\sigma, m \in [0, 1]$. The crossover and mutation rates determine the probability that the given operator is applied to a given population. The crossover operator C_σ describes how sample solutions are recombined to generate new solutions for the next population. The mutation operator M_m describes random distortions to the elements of a population and is particularly significant for the convergence of the GA, as it ensures that the objective space $\mathcal{X}$ is searched comprehensively and that the limit $\mathcal{P}^*$ is initialization-independent. Last, the fitness selection operator F allocates a fitness value to the population members and selects those with the highest values to progress to the next generation.

In this work, simulated binary crossover [47, 48] and polynomial mutation [49, 50] are employed as crossover and mutation operators, respectively. For fitness evaluation, we use the FE model of the quadrupole to compute the magnetic field distribution in the magnet and evaluate the aperture field quality, which in turn determines the fitness of a given population. As a selection operator, we use binary tournament selection [51], due to its ease of implementation and robustness against stochastic noise.

3.2 Non-dominated sorting genetic algorithms & NSGA-III

As noted before, GAs were originally developed to solve single-objective optimization problems. Therefore, they cannot address a number of issues related to MOO, such as dealing with multiple objective functions and ensuring diversity in the populations. These issues have been addressed with

the introduction of NSGAs [29–32]. In this work, we resort to the so-called NSGA-III algorithm [31, 32], which is briefly discussed in the following.

First, NSGA-III deals with the issue of optimizing numerous objective functions by preferentially handling solutions that dominate other members of a population according to definition (14), by using *non-dominated sorting*. Given the current population $\mathcal{P}$, non-domination sorting partitions the population $\mathcal{P} = \mathcal{F}_1 \cup \cdots \cup \mathcal{F}_{N-1}$ into disjoint sets $\mathcal{F}_i$, which form the hierarchy $\mathcal{F}_1 < \mathcal{F}_2 < \cdots < \mathcal{F}_{N-1}$. This hierarchy is induced according to a domination factor $n_p = 0, 1, ..., N - 1$, which indicates how many solutions from an equal or lower hierarchy level dominate the given solution. The hierarchy construction is as follows: The set $\mathcal{F}_1$ includes $\mathbf{x} \in \mathcal{P}$, which have $n_p = 0$, i.e., they are not dominated by any solution. Then, we consider the set $\mathcal{Q} = \mathcal{P}\backslash\mathcal{F}_2$ and decrement the domination factor for $n_p \to n_p - 1$ for all $q \in \mathcal{Q}$ that are dominated by an element of $\mathcal{F}_1$. This process is repeated iteratively, thus yielding a hierarchical set sequence. The sets with lower domination factors qualify to the next population, whereas the sets with higher domination factors are discarded. It is thus ensured that that the solutions propagating to future generations are Pareto optimal with respect to the current population they belong to.

To ensure population diversity, NSGA-III adds another operation to the fitness selection procedure. Therein, the objective vectors $\mathbf{z}$ are normalized to the unit cube by using the ideal objective vector $\mathbf{z}^*$ and the nadir objective vector $\mathbf{z}^{\text{nad.}}$. In that way, it is possible to consider objective functions that are scaled differently. Then, reference points on the unit hypercube are chosen, which lie on a simplex [52]. The reference points typically have a space-filling property and the objective vectors are projected to the reference points. The population members are then determined by an explicit diversity-preserving mechanism.

4 Quadrupole magnet optimization

The MOO concerns maximizing the absolute value of the field gradient g, as introduced in Sect. 2.3, while minimizing the outer radius R of the magnet. The optimization parameters are the six geometrical parameters listed in Table 1 and the current density $\mathbf{j}$. The latter takes values within the interval $[1.0, 20.0]$ A/mm^2 and in the following is denoted with x_7. Then, the MOO problem reads

$$\min_{\mathbf{x}\in\mathcal{X}} \{-|g(\mathbf{x})|, \ R(\mathbf{x})\}, \tag{18}$$

where the feasible decision space is $\mathcal{X} = [a_1, b_1] \otimes \cdots \otimes [a_7, b_7]$.
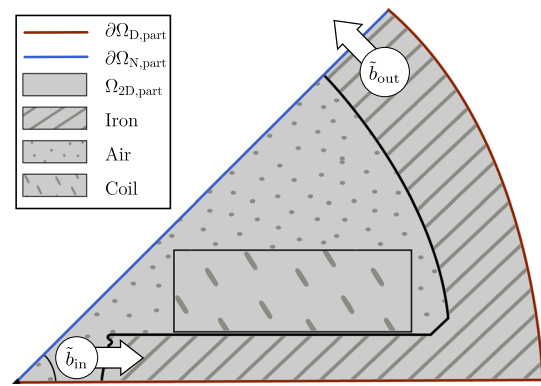

Fig. 3 One-eighth of the 2D quadrupole magnet model (color figure online)

Instead of optimizing the full 2D magnet model shown in Fig. 1, we exploit the three mirror symmetries of the magnet model in order to reduce it to the one-eighth segment depicted in Fig. 3. This model reduction leads to a significant improvement in terms of the computational cost of the finite element method (FEM).

Besides constraints on the geometrical parameters and the current density, we also introduce constraints on the absolute duodecapole gradient g_d, as well as on the saturation behavior of the iron yoke of the magnet, which read

$$|g_d(\mathbf{x})| \le |g(\mathbf{x})|10^{-2}, \tag{19a}$$

$$\tilde{b}_{\text{in}} \le b_{\text{th}}, \tag{19b}$$

$$\tilde{b}_{\text{out}} \le b_{\text{th}}. \tag{19c}$$

Analogously to the quadrupole field gradient g in Equation (11), the duodecapole gradient is given by $g_d = B_6(r_{\text{ref}})$. In any case, the additional constraints demand that the duodecapole gradient g_d should not exceed a certain percentage of the absolute field gradient g, as well as that the magnetic flux density entering the pole nose $\tilde{b}_{\text{in}}$ and the magnetic flux density exiting the yoke bend $\tilde{b}_{\text{out}}$ are bounded by a fixed saturation threshold value b_{th}. The magnetic flux densities $\tilde{b}_{\text{in}}$ and $\tilde{b}_{\text{out}}$ are illustrated in Fig. 3. Both are obtained by post-processing the FE solution a_z.

The solutions to the MOO problem defined by equations (18)-(19) are obtained, as previously noted, using the NSGA-III algorithm. In particular, the implementation of the algorithm which is available in the open-source, Python-based optimization software `pymoo` is used [53].

5 Numerical results

In this section, the numerical results of the MOO are presented, which are additionally employed to identify the best solutions, i.e., the ones corresponding to the most suitable magnet designs. The notion of the best solution is split into:
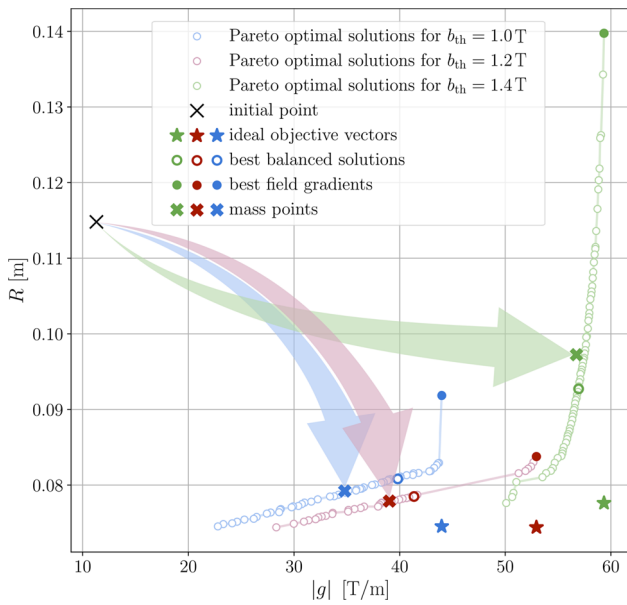
Fig. 4 MOO results for three optimization runs, each corresponding to a different saturation threshold b_{th}. The arrows show the Pareto front movement from the initial point ($\times$) towards the mass point of the final Pareto front ($\ast$) (color figure online)

- *Best balanced solution*, that is, the Pareto optimal solution with the lowest Euclidean distance to the ideal objective vector, where the latter is approximated with respect to the final Pareto front.
- *Best field gradient solution*, that is, the Pareto optimal solution found in the final Pareto front, which results in the highest field gradient.
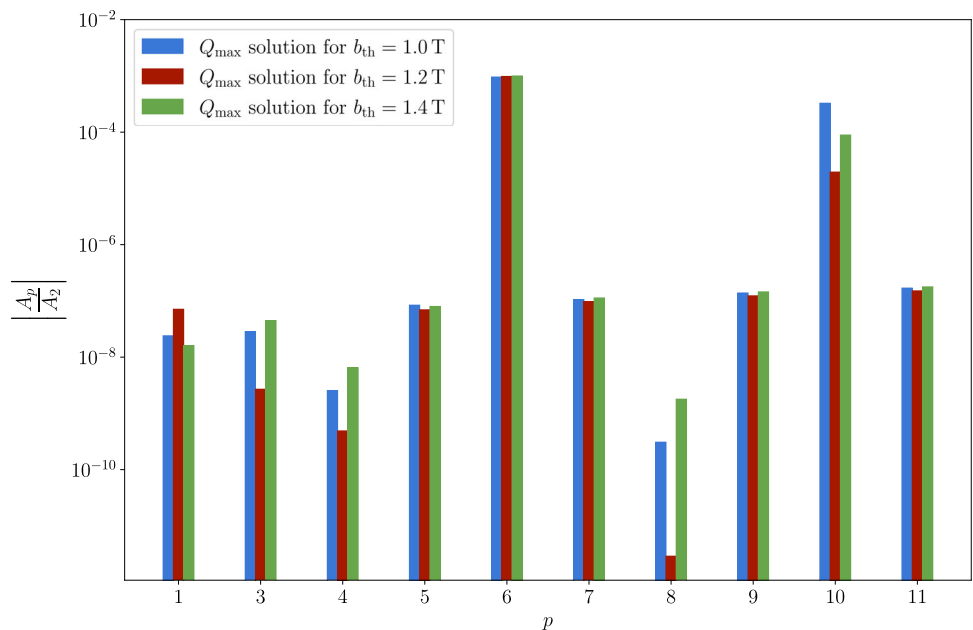
Using NSGA-III with a crossover rate $\sigma = 1.0$ and a polynomial mutation rate $m = 0.1$, each optimization run is performed for $T = 300$ generations, with an initial population of 80 individuals, and an offspring population of 56 individuals. These empirically enforced values remain fixed during several optimization runs, where the influence of different saturation behaviors of the iron is investigated. To analyze the saturation behavior, three optimization runs are performed, within which the saturation threshold b_{th}, which is embedded in the optimization's constraints as in Equations (19), is selected as 1.0T, 1.2T, or 1.4T, respectively. Each optimization run is performed upon the same feasible decision space $\mathcal{X}$. The initial point is chosen to be the center point of $\mathcal{X}$ and represents a naive but admissible choice of geometry with respect to the optimization constraints, see Fig. 4. The associated initial objective values are $R = 0.115$m and $|g| = 11.305$T/m. Here, the initial point serves as a reference point to compare the locations of the different final Pareto fronts.

Figure 4 shows the Pareto front movement and the location of the final Pareto front after $T = 300$ generations for the three chosen saturation thresholds. Therein, the Pareto front movement is obtained by connecting the mass points of the fronts obtained from each generation of the NSGA-III, where the mass point is defined as the mean of all Pareto optimal solutions. As can be seen, both the final Pareto front and the front movement depend strongly on the chosen saturation threshold. For $b_{th} = 1.0$T and $b_{th} = 1.2$T, the final Pareto fronts are biased toward low values of the outer radius R. In contrast, the Pareto front for $b_{th} = 1.4$T is biased toward high field gradient values. As for the individual evolution of the different objective spaces, Fig. 7 in Appendix shows each of
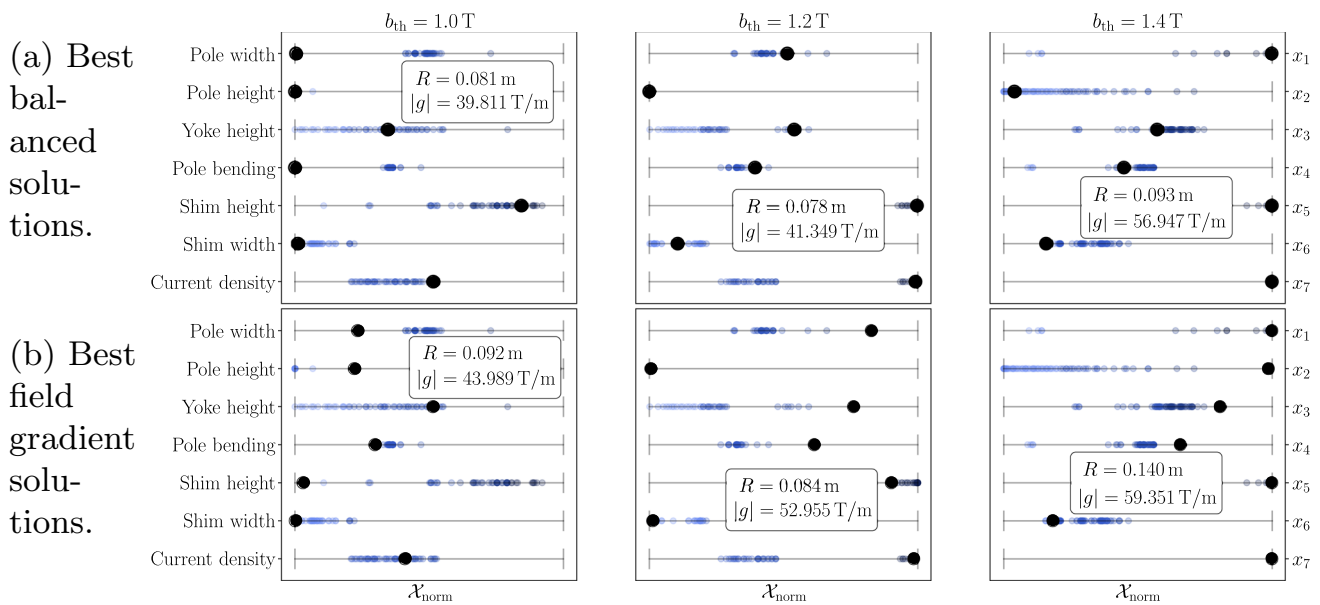
Fig. 5 Relative skew harmonic coefficients of the Pareto front solutions associated with the highest, i.e., worst harmonic distortion factor for each saturation threshold b_{th}, respectively (color figure online)

Fig. 6 Best solutions (normalized) for different saturation threshold values b_{th}. Additionally to the best solutions, the corresponding objective values R and $|g|$ are given. Filled black circles: normalized parameter combinations of the best solutions. Transparent blue-colored circles: normalized parameter combinations of all final Pareto optimal solutions with respect to the different saturation thresholds (color figure online)

the optimization solutions and their Pareto front movements individually.

Figure 5 depicts the relative skew harmonic coefficients with respect to the quadrupole main component, of the Pareto front solutions associated with the highest, i.e., worst harmonic distortion factor Q_{max} for each saturation threshold b_{th}, respectively. Further, it is verified that the Pareto optimal solutions of all optimization runs have a harmonic distortion factor Q below or of order 10^{-4}. This observation is consistent with the theoretical requirements for the harmonic distortion factor of a sufficiently undistorted quadrupole field, as mentioned in Sect. 2.3.

Next, focus is shifted to the best solutions of the final Pareto front for each saturation threshold. For a better visual comparison of the best solutions, the parameter combination corresponding to each solution is normalized to the unit cube $\mathcal{X}_{norm} = [0, 1]^7$. Using this normalization, the parameter distributions and the associated objective values of the best solutions are depicted in Fig. 6. As can be observed, the saturation threshold has a strong influence on the magnet's pole width, both for best balanced and for best field gradient solutions. This is attributed to the fact that higher saturation thresholds lead to a larger pole width design. It is further observed that larger pole widths lead to higher field gradients for both cases of best solutions. The saturation threshold has also a slight to moderate influence on the pole bending design. With regard to the current flow, it can be seen that, for both best solution cases, higher saturation thresholds allow higher current densities, as expected. In the case of the best

balanced solutions (Fig. 6a), it is observed that changes in the saturation threshold have almost no impact on the dimensions of the pole height, yoke height, and the shim geometry. Contrarily, the dimension of the pole height is more important in the case of the best field gradient solution, as can be seen in Fig. 6b. Additionally, the choice of the shim geometry seems to be more important for best field gradient solutions than for best balanced solutions.

6 Conclusion

This work presented a framework for optimizing predominantly the geometrical and secondarily the operational characteristics of a quadrupole magnet. The framework employs a MOO formulation, where two conflicting objectives must be satisfied, namely high magnetic field quality and acceptable production cost. The MOO problem is solved by means of the so-called NSGA-III algorithm, which is a GA suitably modified to address the issues arising in MOO. Therein, a magnetostatic FE model of the magnet is employed in order to assess the quality of the magnetic field in the aperture of the magnet. Finally, the MOO problem is complemented with additional constraints on the duodecapole gradient and the saturation threshold of iron.
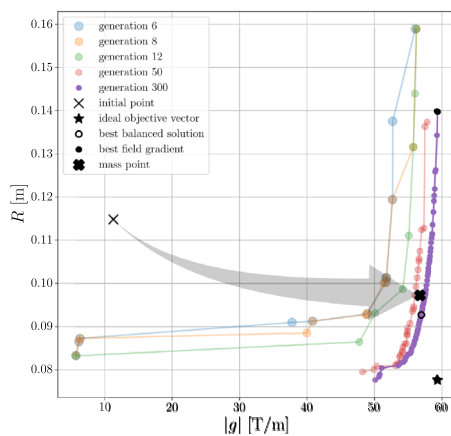
The numerical results indicate that saturation has a major impact on the obtained Pareto optimal solutions. Further analyzing the connection between optimization parameters and Pareto fronts, it is possible to deduce useful information
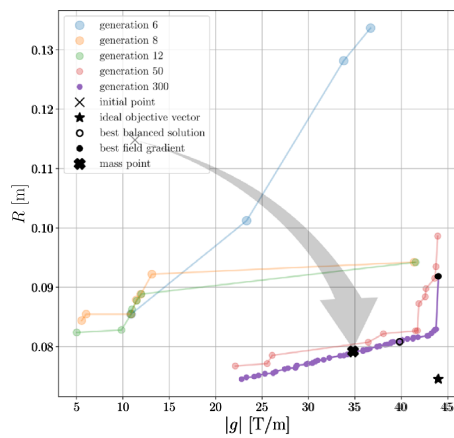
(a) $b_{\text{th}} = 1.0\,\text{T}$.
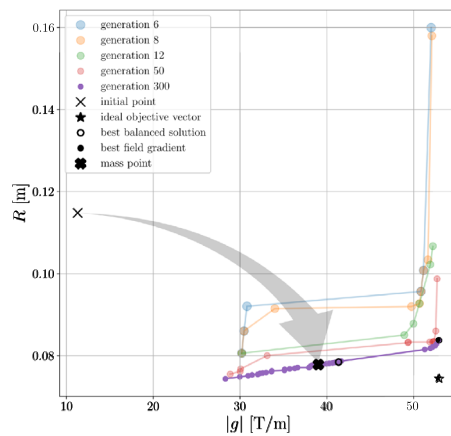
(b) $b_{\text{th}} = 1.2\,\text{T}$.

(c) $b_{\text{th}} = 1.4\,\text{T}$.

Fig. 7 Pareto front movements for each saturation threshold. Colored points: Pareto fronts for different optimization generations. Gray arrow: Pareto front movement from the initial point ($\times$) to the mass point of the final Pareto front ($\maltese$) (color figure online)

regarding the impact of the different geometrical characteristics of the magnet onto the optimization objectives. Importantly, all identified optimal magnet designs lead to a sufficiently low harmonic distortion factor, while it is possible to identify designs with an acceptable balance between field quality and production cost.

Future work should consider the utilization of a 3D magnet model, in order to consider fringe field effects during MOO studies. The impact of eddy currents and power losses should also be taken into account. As a result, MOO problems with $k > 2$ objectives can be formulated and investigated, leading to even more improved magnet designs. To limit the computational burden of MOO, especially for an increased number of objectives, surrogate modeling approaches could be considered [54].

Declarations

Conflict of interest The authors declared no potential conflict of interests with respect to the research, authorship, and/or publication of this article.

Appendix A Pareto Front Movements

See Figure 7.

References

1. Russenschuck S (2011)Field computation for accelerator magnets: analytical and numerical methods for electromagnetic design and optimization. Wiley

2. Conte Mario, MacKay William W (1991) An introduction to the physics of particle accelerators. World Scientific

3. Ahmad Zahoor, Hassan Adnan, Khan Faisal, Lazoglu Ismail (2020) Design of a high thrust density moving magnet linear actuator with magnetic flux bridge. IET Electr Power Appl 14(7):1256–1262

4. Kalimov A (2014) Pole shape optimization in multipole magnets. Math Model Meth Appl Sci

5. Vicente Simón-Sempere, Auxiliadora Simón-Gómez, Manuel Burgos-Payán, José-Ramón Cerquides-Bueno (2021) Optimisation of magnet shape for cogging torque reduction in axial-flux permanent-magnet motors. IEEE Trans Energy Conv 36(4):2825–2838

6. Gabriel Ion Ion, Zeger Bontinck, Dimitrios Loukrezis, Ulrich Römer, Oliver Lass, Stefan Ulbrich, Sebastian Schöps, Herbert De Gersem (2018) Robust shape optimization of electric devices based on deterministic optimization methods and finite-element analysis with affine parametrization and design elements. Electr Eng 100(4):2635–2647

7. Pels Andreas, Bontinck Zeger, Corno Jacopo, De Gersem Herbert, Schöps Sebastian (2015) Optimization of a Stern-Gerlach magnet by magnetic field-circuit coupling and isogeometric analysis. IEEE Trans Magn 51(12):1–7

8. Arora Sanjeev (2003) Approximation schemes for NP-hard geometric optimization problems: A survey. Math Program pp. 43–69

9. Mavrotas George, Pechak Olena, Siskos Eleftherios, Doukas Haris, Psarras John (2015) Robustness analysis in multi-objective mathematical programming using Monte Carlo simulation. Eur J Oper Res 240(1):193–201

10. Mikhailov Gennadii A, Sabelfeld Karl K (1992) Optimization of weighted Monte Carlo methods. Springer

11. Barnoon Pouya, Toghraie Davood, Mehmandoust Babak, Fazilati Mohammad Ali, Ali Eftekhari S (2022) Natural-forced cooling and Monte-Carlo multi-objective optimization of mechanical and thermal characteristics of a bipolar plate for use in a proton exchange membrane fuel cell. *Energy Reports*, 8:2747–2761

12. Donnelly Robert A (1987) Geometry optimization by simulated annealing. Chem Phys Lett 136(3–4):274–278

13. Mundim Kleber C, Tsallis Constantino (1996) Geometry optimization and conformational analysis through generalized simulated annealing. Int J Quant Chem 58(4):373–381

14. Hou Edwin SH, Ansari Nirwan, Ren Hong (1994) A genetic algorithm for multiprocessor scheduling. IEEE Transactions on Parallel and Distributed systems 5(2):113–120

15. Schmitt Lothar M (2001) Theory of genetic algorithms. Theoret Comput Sci 259(1–2):1–61

16. Weile Daniel S, Michielssen Eric (1997) Genetic algorithm optimization applied to electromagnetics: A review. IEEE Trans Antennas Propag 45(3):343–353

17. Abdullah Konak, Coit David W, Smith Alice E (2006) Multi-objective optimization using genetic algorithms: a tutorial. Reliab Eng Syst Safety 91(9):992–1007

18. Asselineau Charles-Alexis, Zapata Jose, Pye John (2015) Integration of Monte-Carlo ray tracing with a stochastic optimisation method: application to the design of solar receiver geometry. Opt Expr 23(11):A437–A443

19. Fuat Uler G, Mohammed Osama A, Chang-Seop Koh (1994) Utilizing genetic algorithms for the optimal design of electromagnetic devices. IEEE Trans Magn 30(6):4296–4298

20. Simkin John, Trowbridge Charles W (1992) Optimizing electromagnetic devices combining direct search methods with simulated annealing. IEEE Trans Magn 28(2):1545–1548

21. Mahrach Mohammed, Miranda Gara, León Coromoto, Segredo Eduardo (2020) Comparison between single and multi-objective evolutionary algorithms to solve the knapsack problem and the travelling salesman problem. Mathematics 8(11):2018

22. Gunantara Nyoman (2018) A review of multi-objective optimization: methods and its applications. Cogent Eng 5(1):1502242

23. Justesen Peter Dueholm (2009) Multi-objective optimization using evolutionary algorithms. University of Aarhus, Department of Computer Science, Denmark, 33

24. Luc Dinh The (2008) Pareto optimality. Pareto optimality, game theory and equilibria, pages 481–515

25. Yadav Gyanendra, Resta-López Javier, Welsch Carsten, Xia Guoxing (2020) Geometric optimization study for a dielectric laser accelerator. In Journal of Physics: Conference Series, 1596:012016. IOP Publishing

26. Di Barba P, Mognaschi ME, Sieni E (2020) Many objective optimization of a magnetic micro-electro-mechanical (MEMS) micromirror with bounded MP-NSGA algorithm. Mathematics 8(9):1509

27. Garcia JCS, Tanaka H, Giannetti N, Sei Y, Saito K, Houfuku M, Takafuji R (2022) Multiobjective geometry optimization of microchannel heat exchanger using real-coded genetic algorithm. Appl Therm Eng 202:117821

28. Bizzozero DA, Qiang J, Ge L, Li Z, Ng C-K, Xiao L (2021) Multi-objective optimization with an integrated electromagnetics and beam dynamics workflow. Nucl Inst Meth Phys Res Sect A Accel Spectro Detect Assoc Equip 1020:165844

29. Srinivas Nidamarthi, Deb Kalyanmoy (1994) Multi-objective optimization using non-dominated sorting in genetic algorithms. Evolut Comput 2(3):221–248

30. Deb Kalyanmoy, Pratap Amrit, Agarwal Sameer, Meyarivan TAMT (2002) A fast and elitist multiobjective genetic algorithm: NSGA-II. IEEE Trans Evolut Comput 6(2):182–197

31. Deb Kalyanmoy, Jain Himanshu (2014) An evolutionary many-objective optimization algorithm using reference-point-based non-dominated sorting approach, part I: Solving problems with box constraints. IEEE Trans Evolut Comput 18(4):577–601

32. Jain Himanshu, Deb Kalyanmoy (2013) An evolutionary many-objective optimization algorithm using reference-point based non-dominated sorting approach, part II: Handling constraints and extending to an adaptive approach. IEEE Trans Evolut Comput 18(4):602–622

33. Edelen Auralee, Neveu Nicole, Frey Matthias, Huber Yannick, Mayes Christopher, Adelmann Andreas (2020) Machine learning for orders of magnitude speedup in multiobjective optimization of particle accelerator systems. Phys Rev Accel Beams 23(4):044601

34. Hofler Alicia, Terzić Balša, Kramer Matthew, Zvezdin Anton, Morozov Vasiliy, Roblin Yves, Lin Fanglei, Jarvis Colin (2013) Innovative applications of genetic algorithms to problems in accelerator physics. Phys Rev Spec Topics Accel Beams 16(1):010101

35. Husain Riyasat, Ghodke AD (2018) Constrained multi-objective optimization of storage ring lattices. Nucl Instrum Meth Phys Res Sect A Accel Spectro Detect Assoc Equip 883:151–158

36. Korchuganov VN, Smygacheva AS, Fomin Ye A (2018) Multiobjective optimization of the synchrotron radiation source Siberia-2 lattice using a genetic algorithm. Phys Part Nuclei Lett 15(1):92–96

37. Neveu Nicole, Spentzouris Linda, Adelmann Andreas, Ineichen Yves, Kolano Anna, Metzger-Kraus Christof, Bekas Costas, Curioni Alessandro, Arbenz Peter (2019) Parallel general purpose multiobjective optimization framework with application to electron beam dynamics. Phys Rev Accel Beams 22(5):054602

38. Yang Lingyun, Robin David, Sannibale Fernando, Steier Christoph, Wan Weishi (2009) Global optimization of an accelerator lattice using multiobjective genetic algorithms. Nucl Instrum Meth Phys Res Sect A Accel Spectro Detect Assoc Equip 609(1):50–57

39. Bossavit A (1998) Computational electromagnetism: variational formulations, complementarity, edge elements. Academic Press

40. Jean-Claude Nédélec (1980) Mixed finite elements in $\mathbb{R}^3$. Numerische Mathematik 35(3):315–341

41. Gupta R, Anerella M, Cozzolino J, Erickson B, Greene A, Jain A, Kahn S, Kelly E, Morgan G, Thompson P, Wanderer P, Willen E (1996) Tuning shims for high field quality in superconducting magnets. IEEE Trans Magn 32(4):2069–2073

42. Bec G. Le, Chavanne J, N'gotta P (2014) Shape Optimization for the ESRF II Magnets. In *Proc. 5th International Particle Accelerator Conference (IPAC'14), Dresden, Germany, June 15-20, 2014*, number 5 in International Particle Accelerator Conference, pages 1232–1234, Geneva, Switzerland, July 2014. JACoW. https://doi.org/10.18429/JACoW-IPAC2014-TUPRO082

43. Brauer J (1975) Simple equations for the magnetization and reluctivity curves of steel. IEEE Trans Magn 11(1):81–81

44. Dular P, Geuzaine C, Henrotte F, Legros W (1998) A general environment for the treatment of discrete problems and its application to the finite element method. IEEE Trans Magn 34(5):3395–3398

45. Geuzaine Christophe, Remacle Jean-François (2009) Gmsh: A 3-d finite element mesh generator with built-in pre-and post-processing facilities. Int J Numer Meth Eng 79(11):1309–1331

46. Geuzaine Christophe, Henrotte François, Remacle Jean-François, Marchandise Emilie, Sabariego Ruth (2013) Onelab: open numerical engineering laboratory. In *Colloque National en Calcul des Structures (CSMA), Date: 2013/05/13-2013/05/17, Location: Giens, Var, France*

47. Deb Kalyanmoy, Sindhya Karthik, Okabe Tatsuya (2007) Self-adaptive simulated binary crossover for real-parameter optimization. In *Proceedings of the 9th Annual Conference on Genetic and Evolutionary Computation*, GECCO '07, page 1187–1194, New York, NY, USA, Association for Computing Machinery

48. Deb K, Agrawal RB et al (1995) Simulated binary crossover for continuous search space. Complex Syst 9(2):115–148

49. Golchha A and Qureshi SG (2015) Non-dominated sorting genetic algorithm-II—A succinct survey. Int J Comput Sci Inf Technol 6(1):252–255

50. Yusoff Y, Ngadiman MS, Zain AM (2011) Overview of NSGA-II for optimizing machining process parameters. Procedia Eng 15:3978–3983

51. Miller Brad L, Goldberg David E (1995) Genetic algorithms, tournament selection, and the effects of noise. Complex Syst, 9

52. Das I, Dennis JE (1998) Normal-boundary intersection: a new method for generating the Pareto surface in nonlinear multicriteria optimization problems. SIAM J Optimiz 8(3):631–657

53. Blank J, Deb K (2020) pymoo: multi-objective optimization in Python. IEEE Access 8:89497–89509

54. Loukrezis Dimitrios, De Gersem Herbert (2022) Power module heat sink design optimization with ensembles of data-driven polynomial chaos surrogate models. e-Prime-Adv Electr Eng Electron Energy, page 100059